Materials Advances

ROYAL SOCIETY OF CHEMISTRY

PAPER

View Article Online
View Journal

Cite this: DOI: 10.1039/d6ma00256k

Enhanced structural, NTCR behavior and dielectric polarization in $LiGaP_2O_7$ pyrophosphate: implications for advanced technological applications

Imen Gharbi,[a] Iheb Garoui,[a] Souad Chkoundali,[a] Nazir Mustapha,*[b] Mokhtar Hjiri[b] and Abderrazek Oueslati*[a]

Materials exhibiting negative temperature coefficient of resistance (NTCR) behavior and efficient ionic transport properties are of considerable interest for advanced dielectric and energy-storage applications. In this work, single-phase $LiGaP_2O_7$ pyrophosphate was successfully synthesized using a conventional solid-state reaction route. X-ray diffraction analysis confirmed the formation of a monoclinic structure with the space group $P2_1$, while scanning electron microscopy revealed a polycrystalline morphology with an average grain size of about 2.49 μm. The electrical and dielectric properties were investigated by impedance spectroscopy over a wide frequency range (0.1 Hz–1 MHz) and temperature interval (513–673 K). Nyquist plots demonstrated that the electrical response is mainly governed by grain boundary effects and were successfully fitted using an equivalent circuit based on parallel R//C//Q elements. The compound exhibited a pronounced NTCR behavior associated with a thermally activated hopping process. Dielectric investigations revealed a non-Debye relaxation behavior accompanied by strong frequency dispersion due to Maxwell–Wagner interfacial polarization. A high dielectric permittivity of approximately 6.32×10^4 was obtained at low frequencies. Electric modulus and conductivity analyses indicated that long-range Li^+ ion migration dominates the transport mechanism. The AC conduction mechanism follows the correlated barrier hopping (CBH) model in the temperature range of 513–593 K with an activation energy of about 0.72 eV, while at higher temperatures (613–673 K), the non-overlapping small polaron tunneling (NSPT) model becomes predominant with an activation energy close to 1.19 eV. These findings provide deeper insight into the dielectric relaxation and charge transport mechanisms of pyrophosphate materials and highlight $LiGaP_2O_7$ as a promising candidate for low-frequency dielectric devices, energy-storage systems, and NTC thermistor applications.

Received 23rd February 2026,
Accepted 29th May 2026

DOI: 10.1039/d6ma00256k

rsc.li/materials-advances

1. Introduction

The search for advanced functional materials capable of meeting the rising demands of energy, electronic, and sustainable technologies remains at the forefront of materials science.[1,2] In this pursuit, phosphate-based compounds, particularly pyrophosphates, have emerged as a versatile class of materials due to their structural stability, tunable frameworks, and wide range of physical properties. Their ability to accommodate diverse cations within robust anionic networks allows subtle chemical substitutions to generate profound changes in dielectric, electrical, and electrochemical behavior.[3–6]

Lithium pyrophosphates of general formula $LiM^{3+}P_2O_7$ (M = trivalent metal) exemplify this versatility. They display a broad spectrum of functionalities, including remarkable dielectric response and potential as electrode materials.[7–9] Several studies have highlighted the remarkable dielectric behavior of these materials, particularly in systems containing Cr, Fe, V, or Bi.[10–14] While much attention has been devoted to systems containing Cr, Fe, V, or Bi, the gallium analogue remains largely overlooked. This is noteworthy since Ga^{3+}, with its small ionic radius (0.62 Å in octahedral coordination) and moderate polarizability, provides a unique balance between size, electronic configuration, and chemical behavior. These attributes influence the local coordination geometry and connectivity of the framework, offering the possibility of unconventional physical behavior.[15–17] $LiGaP_2O_7$ crystallizes in the monoclinic $P2_1$

[a] Laboratory of Spectroscopic Characterization and Optical Materials, Faculty of Sciences, University of Sfax, B.P. 1171, 3000 Sfax, Tunisia. E-mail: oueslatiabderrazek@yaoo.fr
[b] Department of Physics, College of Sciences, Imam Mohammad Ibn Saud Islamic University (IMSIU), Riyadh 11623, Saudi Arabia. E-mail: nmmustapha@imamu.edu.sa

space group, is isostructural with $LiFeP_2O_7$ and $LiCrP_2O_7$, and retains thermal stability up to 600 °C.[18] Moreover, its wide band gap (~4.56 eV) suggests promising dielectric and insulating properties. Yet, in contrast to its structural analogues, its dielectric and electrical characteristics have scarcely been investigated. This gap is striking, as related compounds such as $LiFeP_2O_7$ and β-$LiVP_2O_7$ have already demonstrated technological potential, ranging from cathode stability in lithium-ion batteries[19] to high-power electrode behavior in full-cell configurations.[20,21] These examples highlight how the pyrophosphate framework can couple structural stability with functional performance, underscoring the possibility that $LiGaP_2O_7$ may harbor similarly useful, yet undiscovered, properties.

The growing global need for efficient and reliable energy storage has further increased interest in advanced technologies such as all-solid-state batteries, which offer enhanced safety, superior ionic conductivity, and longer operational lifetimes compared to conventional systems.[22,23] This transition is largely driven by the integration of renewable energy and the rapid growth of electric mobility, which demands durable, high-capacity, and cost-effective storage solutions. Since their commercial debut in 1991,[24] lithium-ion batteries have remained dominant due to their high energy density and broad applicability, from portable electronics to grid-scale storage systems.[25]

To evaluate the suitability of $LiGaP_2O_7$ for low-frequency energy storage systems, such as rechargeable lithium-ion batteries, this study aims to deepen our understanding of its dielectric behavior and charge transport mechanisms that govern its behavior, particularly at the microscopic scale. An in-depth evaluation of its electrical conductivity and dielectric performance was conducted across a wide frequency spectrum (0.1 Hz to 1 MHz) and within a temperature range of 513–673 K. In addition to its energy storage potential, dielectric spectroscopy serves as a powerful tool for probing the negative temperature coefficient (NTC) behavior in pyrophosphate compounds.[4,5] Materials exhibiting NTC characteristics are increasingly important for high-temperature applications, particularly in thermal sensors.[26] NTC thermistors, resistors whose resistance decreases with temperature, are widely used in modern electronics for temperature monitoring, circuit protection, and process control, spanning fields such as aerospace, automotive, pressure sensing, and fluid flow monitoring.[27,28]

Even though a number of $LiM^{3+}P_2O_7$ pyrophosphate compounds have been reported in the literature, most of the available studies are mainly devoted to their structural features and, in certain cases, their optical behavior, whereas their dielectric response and charge transport properties have not been extensively investigated. Among them, $LiGaP_2O_7$ in particular has received only limited attention regarding its electrical characteristics, despite its importance within the $LiM^{3+}P_2O_7$ structural family. Therefore, the present work is dedicated to a detailed study of the dielectric properties as a function of frequency and temperature, together with an analysis of the AC and DC conduction mechanisms in $LiGaP_2O_7$. A comparative discussion with related pyrophosphate materials is also provided, in order to emphasize the unique relaxation behavior and transport features associated with the Ga^{3+}-based framework. Consequently, this study offers additional insight into the relationship between structure and electrical properties in $LiM^{3+}P_2O_7$-type compounds.

In this work, we report a detailed investigation of the dielectric and electrical properties of $LiGaP_2O_7$ to evaluate its potential for electronic and energy-related applications. The compound was synthesized by the conventional solid-state reaction route using high-purity precursors to obtain a single-phase material.[29,30] Despite its promising features, systematic studies of the dielectric response, electrical behavior, and relaxation dynamics of $LiGaP_2O_7$ remain scarce. To address this, impedance and dielectric spectroscopy were carried out over a broad frequency and temperature range, providing insight into conduction mechanisms, polarization processes, and charge transport pathways. Such analyses are crucial for understanding the material's response to thermal and frequency stimuli and for evaluating its suitability for next-generation energy storage and conversion technologies.

2. Experimental methodology

2.1. Synthesis of $LiGaP_2O_7$ *via* the solid-state reaction method

The $LiGaP_2O_7$ ceramic was synthesized *via* a conventional solid-state reaction method using high-purity precursors: Ga_2O_3, Li_2CO_3, and $NH_4H_2PO_4$, all purchased from Sigma-Aldrich. These were weighed in stoichiometric proportions according to the reaction:

$$4NH_4H_2PO_4 + Li_2CO_3 + Ga_2O_3 \rightarrow 2LiGaP_2O_7 + 6H_2O + CO_2 + 4NH_3 \quad (1)$$

The precursor powders were thoroughly homogenized by manual grinding in an agate mortar for about 3 hours. The obtained mixture was then heated on a hot plate at 300 °C for 8 hours to remove any volatile species, followed by an additional grinding step of 1 hour to ensure uniformity. The dried powder was compacted into 8 mm diameter pellets using a uniaxial pressure of 3 tons per cm^2. These pellets were then sintered at 800 °C for 2 hours in an alumina crucible to promote phase development and improve densification. After sintering, the samples reached a relative density close to 96% of the theoretical value. Finally, both surfaces of the pellets were coated with silver paste to act as electrodes in a parallel-plate geometry. A schematic illustration of the synthesis procedure is presented in Fig. 1.

2.2. Instrumentation and measurement methods

Structural, morphological, vibrational, and electrical characterization techniques were employed to investigate the physical properties of the synthesized $LiGaP_2O_7$ compound. Powder X-ray diffraction (PXRD) was utilized as a reliable method to confirm the crystallinity of the sample. This analysis was performed at room temperature using a Bruker D8 Advance diffractometer, operating within a 2θ range of 5° to 80°, and equipped with a copper anode (CuK_α radiation, λ = 0.15406 Å).

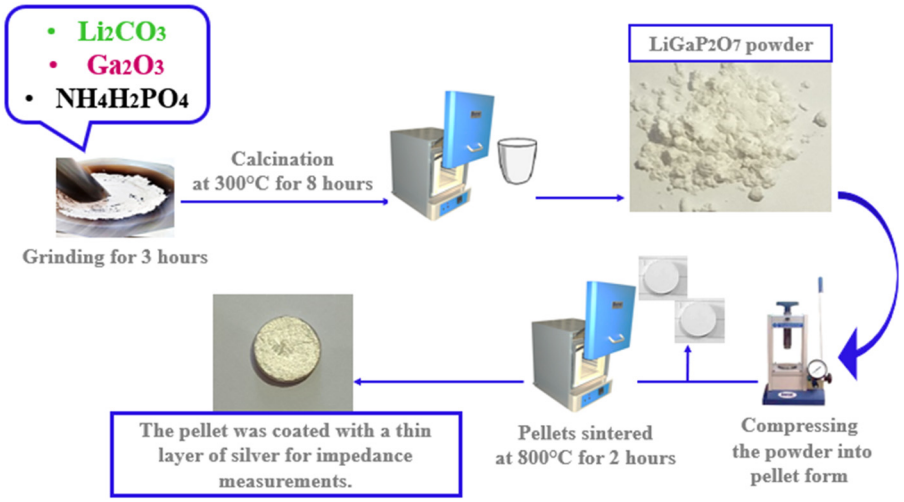

Fig. 1 Schematic representation of the synthesis process of the $LiGaP_2O_7$ compound using the solid-state reaction method.

Microstructural and morphological analyses of the $LiGaP_2O_7$ powder were performed at room temperature using a JEOL JSM-650LV environmental scanning electron microscope (ESEM). The powder was lightly spread onto conductive carbon tape mounted on an aluminum stub and subsequently coated with a thin layer of gold to improve surface conductivity and imaging quality. High-resolution imaging was carried out under high-vacuum conditions with an accelerating voltage of 15 kV, allowing detailed examination of particle size and shape.

Raman spectroscopy was employed to investigate the vibrational properties of the $LiGaP_2O_7$ powder, using a Horiba Jobin-Yvon T64000 triple-grating spectrometer. Spectra were recorded at ambient temperature over the spectral range of 50–1200 cm^{-1}, enabling identification of characteristic vibrational modes associated with the phosphate framework.

Impedance spectroscopy (IS) was employed to investigate the electrical behavior of the $LiGaP_2O_7$ compound, with particular attention to the distinct contributions from grains and grain boundaries. The sample, prepared in disc form (8 mm diameter, 1 mm thickness), was coated on both faces with a thin layer of silver conductive paste to ensure stable and reproducible electrical contact. Measurements were performed in a cryostat chamber enabling precise temperature control from 513 to 673 K. Temperature stability was maintained within ±0.5 K, with a resolution of 0.1 K, using a high-precision controller equipped with a closed-loop feedback system to ensure uniform thermal distribution. Electrical characterization was conducted under ambient atmosphere using a Solartron 1260 impedance/gain-phase analyzer, applying a 1 V excitation across a broad frequency range from 0.1 Hz to 1 MHz.

3. Results and discussion

3.1. Analysis of structural properties

The $LiGaP_2O_7$ pyrophosphate was successfully synthesized, and its crystalline phase was examined by powder X-ray diffraction (PXRD) analysis. As shown in Fig. 2(a), the experimental PXRD

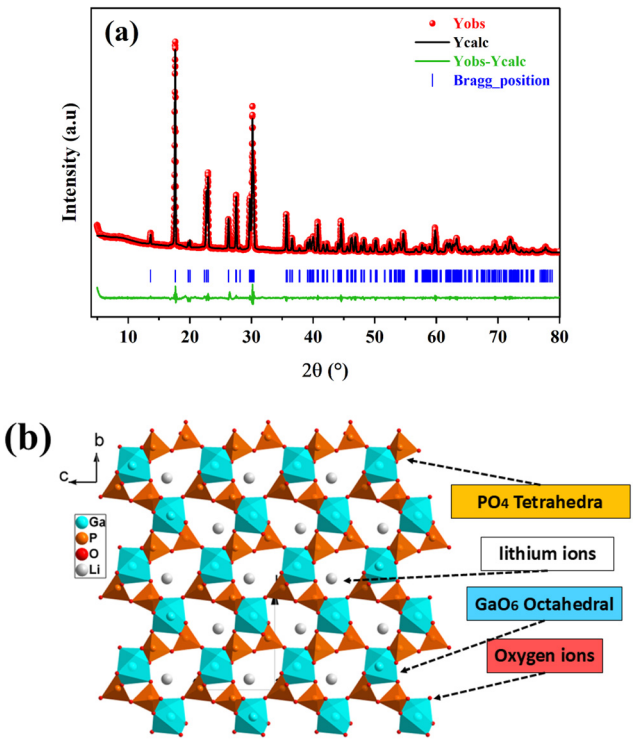

Fig. 2 (a) Profile refinement of the PXRD data. (b) Crystal structure model of $LiGaP_2O_7$.

pattern confirms the formation of a single-phase material, with sharp and well-defined diffraction peaks indicative of good crystallinity and a polycrystalline nature.

Rietveld refinement was performed using the FullProf software[31] to confirm the structural details. The refinement converged smoothly, yielding a good fit between the observed and calculated patterns, as illustrated in Fig. 2(a). The best agreement was obtained, assuming a monoclinic crystal system with the $P2_1$ space group. The low value of the goodness of fit indicator (χ^2), along with minimal differences in the

Table 1 Refined structural parameters of the $LiGaP_2O_7$ compound at room temperature

Formula	$LiGaP_2O_7$
Molar mass	250.60 g mol^{-1}
Crystal system	Monoclinic
Space-group	$P2_1$
Cell parameters	a = 4.762 ± 0.002 Å b = 7.959 ± 0.003 Å c = 6.876 ± 0.002 Å β = 108.978 ± 0.02°
Cell volume	246.3 ± 0.2 $Å^3$
Z	2
R-factors	
$R_p/R_{wp}/R_{exp}$ (%)	26.5/28.4/25.70
χ^2	1.26
D_SC (nm)	60

Yobs–Ycalc profile and accurately matched Bragg peak positions, confirms the structural integrity and phase purity of the synthesized compound. The refined crystallographic parameters (a, b, c, β), unit cell volume (V), reliability factors (R-factors), and goodness of fit (χ^2) are summarized in Table 1. These values are in good agreement with those previously reported by Y. Li *et al.* in 2019,[18] further validating the structural model used.

To estimate the average crystallite size of $LiGaP_2O_7$, the classical Debye–Scherrer formula was applied to the most intense diffraction peak located at $2\theta = 17.632°$. The calculation was carried out using the Debye–Scherrer equation, which is commonly used to evaluate crystallite dimensions based on PXRD data:[32]

$$\text{D\_SC} = \frac{0.9\lambda}{\beta\cos(\theta)} \quad (2)$$

In this equation, λ is the X-ray wavelength (1.54056 Å for Cu Kα radiation), θ is the Bragg angle, and β is the full width at half maximum (FWHM) of the selected diffraction peak (in radians). Based on this calculation, the average crystallite size of the $LiGaP_2O_7$ sample was found to be approximately 60 nm.

Crystallite size plays a significant role in determining the material's dielectric, conduction, and relaxation properties, as these are closely tied to the microstructural characteristics of the ceramic. Parameters such as crystallite size, grain boundaries, and porosity can critically affect the charge transport mechanisms and relaxation behavior in pyrophosphate-based materials.[33,34]

The crystal structure of $LiGaP_2O_7$ consists of corner-sharing PO_4 tetrahedra forming P_2O_7 pyrophosphate groups, which link with GaO_6 octahedra to create layered GaP_2O_{11} sheets. These layers are connected through bridging oxygen atoms, resulting in a stable three-dimensional framework. Lithium ions occupy large interlayer voids, leading to a distorted Li–O coordination environment that enables efficient Li^+ migration through open diffusion channels.[18] This unique structural arrangement supports both mechanical stability and effective ionic transport, highlighting the material's promise for solid-state electrolyte and lithium-ion battery applications.

3.2. Microstructural analysis

Fig. 3(a) shows the SEM image of the synthesized $LiGaP_2O_7$ powder, recorded at a magnification of 2000×. The microstructure reveals a highly agglomerated morphology with irregularly shaped particles forming loosely packed clusters. This type of aggregation is commonly observed in powders obtained *via* solid-state reaction, where grain growth and surface energy minimization lead to particle clustering.

A quantitative analysis of the particle size was carried out using ImageJ, an image processing software. As illustrated in Fig. 3(b), the grain size distribution was extracted from the SEM image and fitted with a lognormal distribution function, reflecting the asymmetry observed in particle size distribution. The average particle size was found to be approximately 2.49 μm, indicating a moderately broad size dispersion across the sample.

The average particle size observed is considerably larger than the crystallite size of approximately 60 nm estimated from X-ray diffraction using the Debye–Scherrer equation. This difference indicates that each particle observed in the SEM images is an aggregate composed of multiple smaller crystallites.[34] Such microstructures can influence key material behaviors, including densification dynamics during sintering, ionic transport efficiency, and interfacial polarization effects. Overall, the morphological analysis offers valuable insights into the powder's microstructural characteristics, which are critical for tailoring the material's performance in applications such as solid-state electrolytes, sensors, or electrochemical devices.

3.3. Raman spectroscopy and vibrational mode analysis

Fig. 4 presents the Raman spectrum of the $LiGaP_2O_7$ compound, which exhibits a series of well-defined bands that can be attributed to the internal and external vibrational modes of the pyrophosphate ($P_2O_7^{4-}$) groups. The Raman band assignments of the pyrophosphate compounds follow an order of diphosphate vibrations arranged by decreasing frequency:

$$\nu_{as}(PO_3) > \nu_s(PO_3) > \nu_{as}(POP) > \nu_s(POP) > \delta_{as}(PO_3) > \delta_s(PO_3) > \delta_s(POP).$$

Note that ν_{as} and ν_s are relevant to the asymmetric and symmetric stretching vibrations of terminal (PO_3) and bridging (P–O–P) bonds, respectively, while δ refers to the corresponding bending modes, which generally occur at lower frequencies.

The most intense band observed at 1112 cm^{-1}, as well as the ones located at 1146 cm^{-1} and 1079 cm^{-1}, are assigned to the asymmetric stretching vibration (ν_{as}) of terminal PO_3 groups. Additional stretching vibrations appear at 1043 cm^{-1}, corresponding to symmetric stretching (ν_s) of terminal PO_3 groups. The weaker bands at 968 cm^{-1} and 930 cm^{-1} are likely associated with the asymmetric stretch of the P–O–P linkage (ν_{as}(P–O–P)), while the one at 772 cm^{-1} corresponds to the symmetric stretch of the P–O–P linkage (ν_s(P–O–P)). As for the band located at 625 cm^{-1}, it is attributed to the asymmetric bending of PO_3 groups. Moreover, bands around 568, 544, 429,

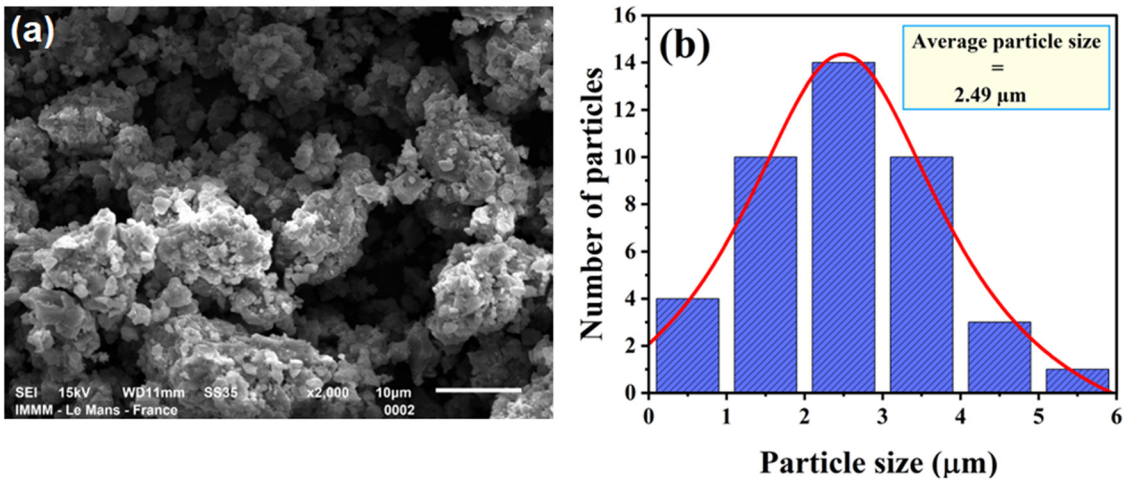

Fig. 3 (a) SEM image (10 µm scale) and (b) corresponding grain size distribution of the $LiGaP_2O_7$ compound.

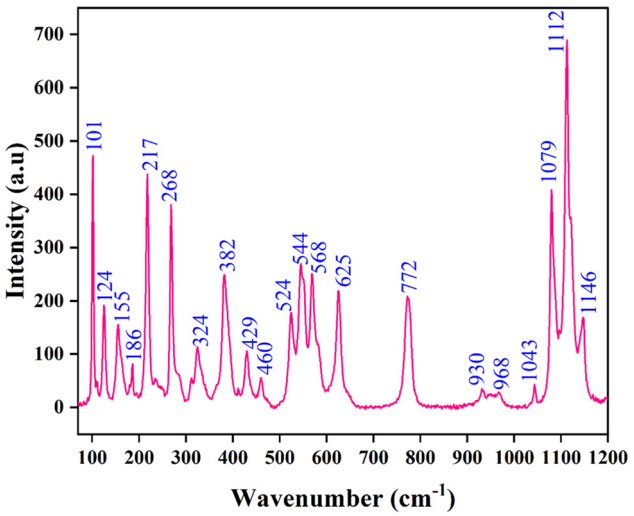

Fig. 4 Raman spectrum of the $LiGaP_2O_7$ pyrophosphate.

460, 382, and 324 cm^{-1} are attributed to the symmetric bending of PO_3 groups. The lower wavenumber region (101–268 cm^{-1}) corresponds to lattice vibrations and external modes where distinct and well-resolved bands are observed, indicating the high crystallinity of the samples synthesized *via* the solid-state method.

Overall, the spectral features are consistent with the vibrational signatures reported for pyrophosphate-based compounds, confirming the integrity of the $P_2O_7^{4-}$ structural motif in the $LiGaP_2O_7$ compound. The assignments were determined based on previously published Raman studies on diphosphates.[3,5,35–38]

3.4. Negative temperature coefficient of resistance (NTCR) behavior

Following the structural and morphological characterization studies, the electrical properties of the material were examined using complex impedance spectroscopy (CIS) over a frequency range of 1 Hz to 1 MHz and a temperature span from 513 K to 673 K, with 20 K increments. This technique links an electrical circuit model with the actual response of the material, offering valuable insights into microstructural contributions such as grains, grain boundaries, and electrode material interfaces.[39–41] CIS is particularly effective for investigating materials that exhibit negative temperature coefficient of resistance (NTCR) behavior,[42] as it enables the identification of temperature-dependent conduction mechanisms through detailed impedance parameter analysis. The complex impedance is represented as:

$$Z^*(\omega) = Z'(\omega) + jZ''(\omega) \quad (3)$$

where Z' and Z'' represent the real and imaginary components of the impedance, respectively.

Fig. 5(a) displays the frequency dependence of the real part of the impedance (Z') across the studied temperature range. The spectra exhibit two distinct regimes: (i) a low-frequency plateau where Z' remains nearly constant, associated with DC conduction, and (ii) a high-frequency dispersive region, indicative of AC conduction. The DC response stems from long-range charge transport *via* successful hopping mechanisms, allowing carriers to migrate and stabilize at adjacent sites.[5,34] In contrast, the frequency-dependent AC region arises from localized hopping processes, where carriers oscillate within limited distances under the influence of the alternating field, resulting in a dispersive impedance response. These two transport regimes reflect the dual conduction nature of the material: DC conduction dominates at low frequencies, while AC conductivity becomes prominent with increasing frequency. Notably, the onset frequency for the plateau shifts toward higher values with increasing temperature, suggesting thermally activated relaxation processes. At high frequencies, Z' decreases significantly, reflecting reduced resistance due to enhanced carrier mobility. Additionally, in the low-frequency region, the decreasing Z' with rising temperature highlights the NTCR behavior characteristic of semiconducting systems,[41] thus confirming the potential thermistor-like nature of the material.

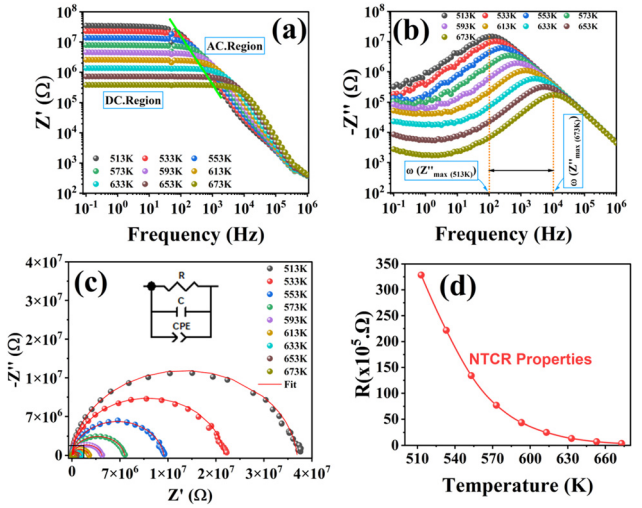

Fig. 5 (a) Frequency dependence of the real (Z') and (b) imaginary ($-Z''$) parts of the impedance at various temperatures. (c) Nyquist plots at different temperatures with the corresponding equivalent circuit model (inset). (d) Temperature dependence of the grain boundary resistance of the $LiGaP_2O_7$ compound.

Fig. 5(b) displays the frequency dependence of the imaginary part of the impedance ($-Z''$) across the studied temperature range. Each spectrum exhibits a distinct relaxation peak, corresponding to the characteristic frequency (f_{max}) at which the dielectric relaxation process is most active. These peaks result from the interplay between resistive and capacitive components, marking the transition from capacitive to conductive behavior. As the temperature increases, the relaxation peak systematically shifts toward higher frequencies and decreases in magnitude.

This behavior indicates a thermally activated relaxation mechanism, where the mobility of charge carriers improves with temperature, leading to shorter relaxation times. Moreover, the broad and asymmetric nature of the peaks suggests a non-Debye type relaxation, typical of disordered or polycrystalline materials, where a distribution of relaxation times exists due to structural or compositional inhomogeneities.[4,5,37]

Fig. 5(c) presents the Nyquist (Cole–Cole) plots for the $LiGaP_2O_7$ compound at various temperatures, revealing depressed semicircular arcs characteristic of a non-Debye relaxation mechanism. The flattening of these arcs implies a wide distribution of relaxation times, commonly attributed to microstructural heterogeneities such as grains and grain boundaries. Notably, the semicircle diameter decreases with increasing temperature, indicating a reduction in resistance due to thermally enhanced charge carrier mobility.

The electrical response of $LiGaP_2O_7$ is strongly influenced by its microstructural features. SEM analysis reveals a polycrystalline morphology characterized by relatively large grains ($\sim$2.49 μm), which are discrete crystalline domains separated by grain boundary regions, narrow disordered interfacial zones where atomic periodicity is disrupted and structural discontinuities arise. These grain boundaries act as energetic barriers to charge carrier transport due to the accumulation of space charge, lattice mismatch, and defect states that locally modify the electrochemical potential. As a result, the overall impedance behavior of $LiGaP_2O_7$ is predominantly governed by grain boundary contributions.[43]

In the low-frequency region of the impedance spectrum, mobile charge carriers (ions or polarons) do not possess sufficient energy to overcome grain boundary barriers within the timescale of the applied alternating field. Consequently, these carriers accumulate preferentially at grain boundary interfaces, forming space-charge double layers that behave as capacitive elements. This accumulation leads to pronounced polarization effects, a phenomenon in which mobile or bound charges are displaced over short distances under an external electric field, resulting in an enhanced dielectric constant and increased resistance. These features are clearly reflected in the Nyquist plots as large, partially resolved semicircular arcs associated with grain boundary relaxation processes.

The observed non-ideal behavior is characteristic of a non-Debye relaxation process, in which polarization does not follow a single exponential decay. Instead, it exhibits a distribution of relaxation times arising from structural and chemical heterogeneity at grain boundaries, including variations in grain size, orientation, defect density, and local composition. This deviation from ideal Debye behavior is typically modeled using constant phase elements (CPEs) in the equivalent circuit, which more accurately describe the frequency dispersion of the dielectric response than ideal capacitors. A higher density of grain boundaries (associated with smaller grain sizes) generally enhances carrier scattering and polarization effects, whereas fewer but well-defined boundaries, as observed here for relatively large grains ($\sim$2.49 μm), lead to more distinct and well-resolved semicircular arcs in the Nyquist plots. Ultimately, the grain boundary network serves as the dominant factor governing the electrical conduction pathway, controlling both the magnitude of the total resistance and the frequency-dependent relaxation behavior across the impedance spectrum.[44]

To interpret the impedance response, the spectra were modeled using an equivalent circuit, shown in the inset of Fig. 5(c). The fitting, performed *via* ZView software,[37] employs a parallel combination of a resistor (R), a capacitor (C), and a constant phase element (CPE), which accounts for the non-ideal dielectric behavior observed. The CPE's impedance is given by the following expression:

$$Z_{CPE} = \frac{1}{(j\omega Q)^{\alpha}} \quad (4)$$

where Q is the pseudo-capacitance and α is a dimensionless exponent ($0 \leq \alpha \leq 1$): a pure resistor for $\alpha = 0$, an ideal capacitor for $\alpha = 1$, and a Warburg diffusion element when $\alpha = 0.5$.

The fitted parameters, summarized in Table 2, include resistance, capacitance, and CPE components for each temperature. The extracted capacitance values fall in the range of 10^{-11} F (grain capacitance, C_g) to 10^{-10} F (grain boundary capacitance, C_{gb}). In particular, the χ^2 values were found to

Table 2 Electrical parameters, deduced using the Z-View software, at selected temperature values

T (K)	R ($\times 10^5$ Ω)	C_g ($\times 10^{-11}$ F)	C_{gb} ($\times 10^{-10}$ F)	α	χ^2
513	328.41	2.634	0.394	0.895	0.00665
533	221.76	2.274	0.444	0.913	0.00298
553	134.1	2.733	0.573	0.864	0.00198
573	76.928	2.893	0.773	0.821	0.00206
593	43.3579	3.043	1.131	0.784	0.00076
613	24.98	3.138	1.672	0.743	0.00066
633	13.361	3.197	2.193	0.712	0.00075
653	7.140	3.232	2.238	0.706	0.00083
673	3.789	3.189	1.364	0.750	0.00132

be very low, ranging from 6.65×10^{-3} at 513 K to 6.5×10^{-4} at 593 K, confirming the excellent agreement between the experimental and fitted impedance data over the investigated temperature range.

These values indicate that at higher frequencies, conduction is predominantly through the grains, while grain boundary effects become significant at lower frequencies. The latter leads us to conclude that the impedance spectra are dominated by grain boundary contributions, as indicated by the large semicircle observed in the Nyquist plots, the high capacitance values, and the depressed nature of the arcs reflecting non-Debye relaxation. Although grain effects are present, particularly at higher frequencies, grain boundary conduction is the prevailing mechanism under the investigated conditions. The dual nature of conduction pathways in the material supports its classification as a thermally activated semiconductor with complex dielectric dynamics.

Fig. 5(d) displays the temperature dependence of grain boundary resistance, which shows a clear decreasing trend with rising temperature. This behavior supports a thermally activated transport mechanism and highlights the semiconducting properties of the $LiGaP_2O_7$ compound.

The impedance measurements obtained at 593 K show an excellent agreement between the experimental spectra and the simulated data using the (R//C//CPE) equivalent circuit model (Fig. 6), demonstrating the suitability of the proposed electrical representation. The very small chi-squared value ($\chi^2 = 7.62 \times 10^{-4}$) confirms the high fitting precision and the strong consistency between the calculated and experimental impedance responses.

In addition, the Bode representations, including the variation of $|Z|$ and phase angle with frequency, further validate the fitting procedure since the theoretical curves accurately reproduce the experimental behavior throughout the investigated frequency domain. The progressive reduction of the impedance magnitude at higher frequencies reflects a thermally activated conduction process,[45,46] whereas the broad relaxation feature observed in the phase angle spectra indicates a distribution of relaxation times, typical of polycrystalline systems where grain boundary effects dominate the electrical transport behavior.

To further assess the material's performance, we examined its electrical stability by calculating the stability factor (SF) using the following equation:[42]

$$\mathrm{SF} = \log\left(\frac{R_{\max}}{R_{\min}}\right) \quad (5)$$

The stability factor (SF) is calculated as the ratio between the maximum and minimum resistivity (R_{max}/R_{min}) measured over a specified temperature interval. This parameter offers a meaningful assessment of how much the material's resistivity changes with temperature, helping to distinguish between stable and fluctuating electrical behavior. A lower SF value indicates greater electrical stability, which is advantageous for real-world applications. For the compound under investigation, the computed SF value is 4.94, suggesting a relatively consistent resistivity response across the studied temperature range.

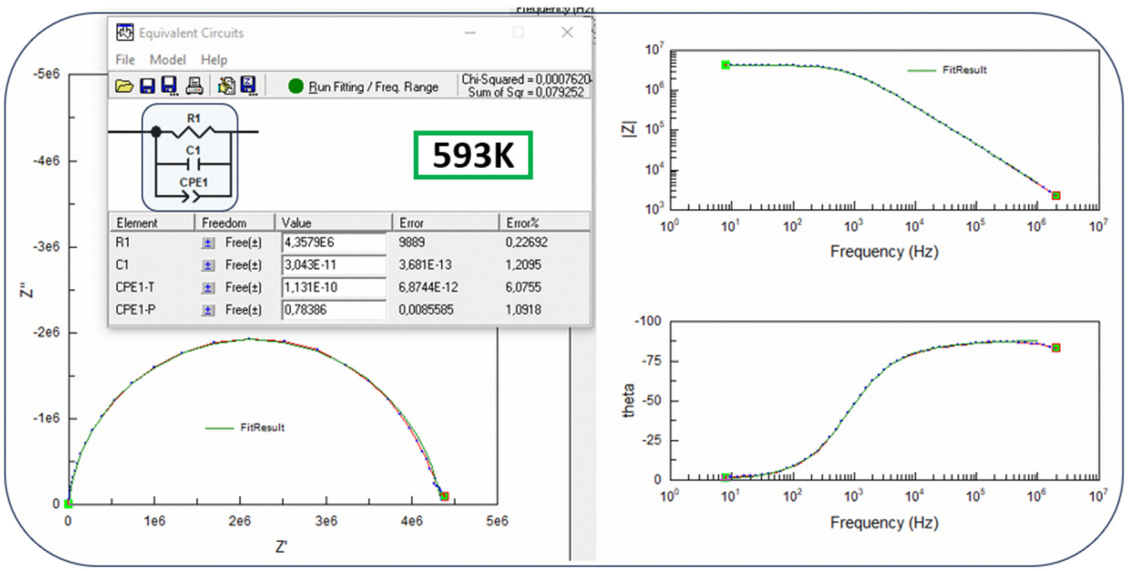

Fig. 6 Experimental and fitted impedance spectra of $LiGaP_2O_7$ at 593 K using the (R//C//CPE) equivalent circuit model: Nyquist plot, variation of impedance magnitude ($|Z|$) with frequency, and phase angle as a function of frequency.

Compared to values reported in similar studies, this finding reinforces the suitability of the $LiGaP_2O_7$ as a potential NTC thermistor material,[41,42,47] and it opens up the possibility for application in lithium-ion batteries (particularly as a cathode or solid electrolyte material), pending further investigation of its lithium-ion conductivity and intercalation capabilities.

3.5. Electrical conduction properties

Presenting electrical conductivity (σ) across different frequencies and temperatures is essential for evaluating the electrical behavior of the sample and determining the underlying conduction mechanism. Conductivity can be calculated using the following equation:

$$\sigma = \frac{e}{s}\frac{Z'}{(Z'^2 + Z''^2)} \quad (6)$$

where "*e*" and "*s*" refer to the thickness and area of the pellet, respectively.

Fig. 7(a) illustrates the variation of electrical conductivity of the $LiGaP_2O_7$ compound as a function of frequency across the investigated temperature range. The observed conductivity behavior can be divided into two distinct regions. At low frequencies (<100 Hz), the electrical conductivity is almost frequency-independent, forming a plateau that corresponds to the DC conductivity region. In this range, charge carriers are able to move to adjacent vacant sites with minimal influence from the external electric field. As the frequency increases beyond a characteristic threshold (the hopping frequency, f_H), typically from >100 Hz up to approximately 10 kHz depending on temperature, the conductivity begins to deviate from this plateau. In this higher-frequency region, the AC conductivity increases with frequency, indicating enhanced hopping dynamics of the charge carriers. This trend reflects the onset of additional charge transport mechanisms becoming active at higher frequencies. Therefore, the observed changes in conductivity across the examined temperature range can be described by Jonscher's universal power law:[48]

$$\sigma(T,\omega) = \sigma_{dc}(T) + \sigma_{ac}(\omega) = \sigma_{dc}(T) + A\omega^{s(T)} \quad (7)$$

According to Jonscher's law, *A* serves as a scaling factor that determines the magnitude of the frequency-dependent component in the conductivity equation. It indicates how significantly conductivity changes with frequency and is linked to the material's polarizability.[49] Higher *A* values imply improved charge carrier mobility and concentration. As presented in Table 3, parameter *A* increases with temperature, reflecting enhanced charge transport. Similarly, the direct current conductivity (σ_{dc}) also rises with temperature, confirming the semiconducting nature of the compound. As for the exponent "*s*", it is a dimensionless factor that characterizes the interaction level between mobile ions and the surrounding lattice environment.[50]

Fig. 7(b) presents the temperature-dependent evolution of the frequency exponent "*s*" for the studied compound. In the temperature range of 513–593 K, a gradual decrease in the value

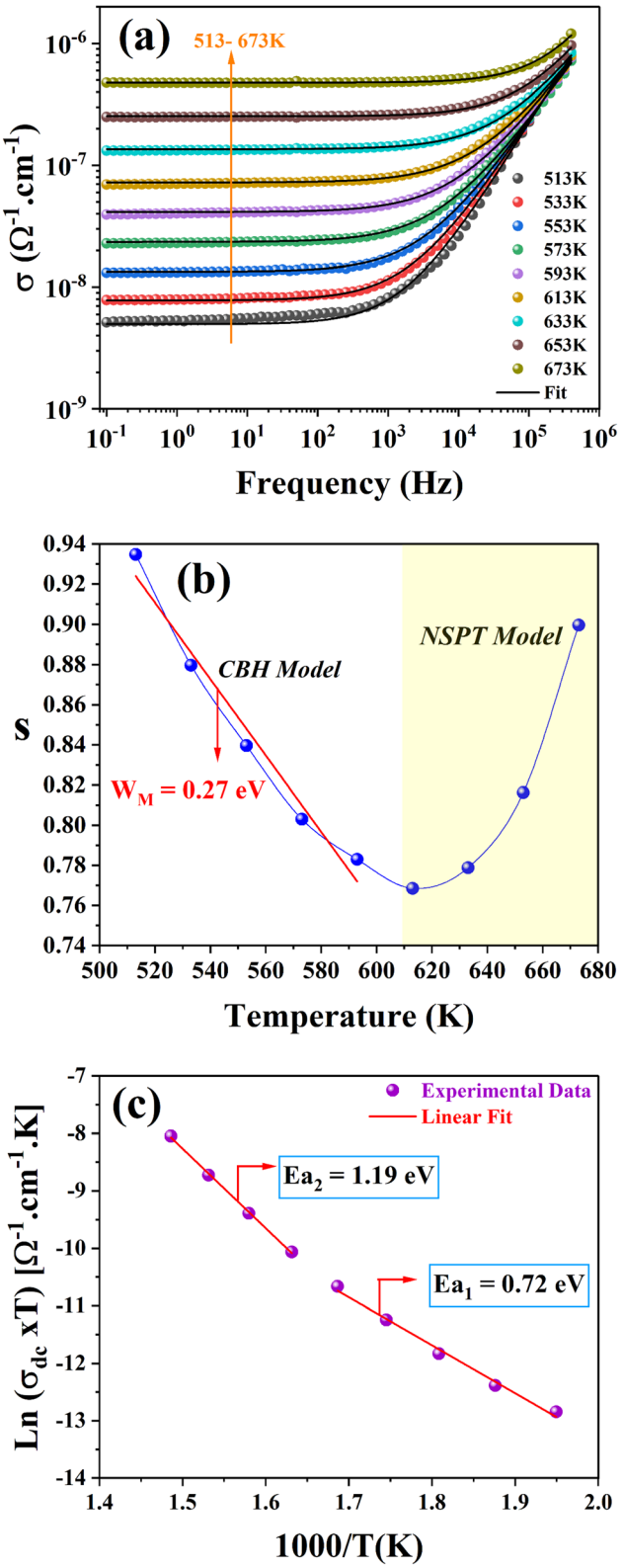

Fig. 7 (a) Frequency-dependent AC conductivity of the $LiGaP_2O_7$ compound at various temperatures. (b) Temperature dependence of the frequency exponent "*s*". (c) Plot of $\ln(\sigma_{dc}\cdot T)$ *versus* inverse temperature (1000/*T*) for the $LiGaP_2O_7$ compound.

Table 3 The list of parameters obtained by fitting the Jonscher function to the frequency dependent conductivity (σ) data

T (K)	σ_{dc} ($\times 10^{-9}$ Ω^{-1} cm^{-1})	$A \times 10^{-12}$	S
513	5.148	0.462	0.935
533	7.830	0.891	0.880
553	13.125	1.475	0.840
573	22.788	2.126	0.803
593	39.442	2.864	0.783
613	69.442	3.379	0.769
633	132.190	2.893	0.779
653	249.360	1.793	0.816
673	476	0.628	0.900

of s is observed as the temperature increases, with all values remaining below 1. This behavior is characteristic of the correlated barrier hopping (CBH) model,[51] which suggests that charge transport occurs through a single-polaron or bipolaron hopping mechanism over a Coulombic potential barrier between localized trapping sites. However, in the higher temperature interval of 613–673 K, the exponent "*s*" increases progressively with temperature. This behavior aligns with the non-overlapping small polaron tunneling (NSPT) model,[52] indicating a transition in the conduction mechanism. In the context of the CBH model, the exponent "*s*" can be calculated using the following equation:[53]

$$s = 1 - \frac{6k_B T}{W_M} \quad (8)$$

Fig. 7(b) illustrates the linear fitting of the frequency exponent *s* as a function of temperature in the range of 513–593 K, based on the correlated barrier hopping (CBH) model. This analysis enabled the estimation of the self-trapping energy W_m, which quantifies the energy required for a charge carrier to become localized. The obtained value of W_m is approximately 0.27 eV.

Similarly, the parameter "*A*" increases with temperature from 513 K to 613 K and then decreases at higher temperatures, exhibiting a thermal behavior similar to that of the exponent "*s*". This behavior suggests that the conduction process is thermally activated up to 613 K, where the increased thermal energy enhances charge carrier mobility and hopping probability between localized states. At temperatures above 613 K, the decrease in *A* confirms a modification of the dominant conduction mechanism, consistent with a transition from the correlated barrier hopping (CBH) model to the non-small polaron tunneling (NSPT) mechanism, as already evidenced by the temperature dependence of the exponent "*s*". Such behavior is typical in disordered or polycrystalline materials, where the increase in temperature can modify the potential barrier height and carrier localization, thus altering the frequency response of the AC conductivity.

Fig. 7(c) presents the temperature dependence of Ln ($\sigma_{dc} \times T$) at a low frequency (f = 0.1 Hz) for the $LiGaP_2O_7$ compound, to evaluate the activation energy associated with DC conductivity. The resulting plots were successfully fitted using the small polaron hopping model proposed by Mott and Davis:[54]

$$\sigma_{dc} = \frac{\sigma_0}{T} \exp\left(\frac{-E_a}{k_B \times T}\right) \quad (9)$$

where E_a represents the activation energy, σ_0 denotes the pre-exponential factor, and k_B is the Boltzmann constant.

A noticeable variation in the slope of the Mott and Davis plot reveals the existence of two separate activation energies: E_{a1} = 0.72 eV within the temperature interval 513–593 K, and E_{a2} = 1.19 eV in the range 613–673 K. This shift in slope confirms the change in the dominant charge transport mechanism. The observed discontinuity is likely to result from either a reallocation of mobile ions between distinct lattice positions or an alteration in their immediate structural surroundings.[5] Such transformations can lead to an increase in the energy required for ionic movement, thereby explaining the rise in activation energy. The transition in the conduction mechanism around ~613 K can be explained by the modification of the charge transport dynamics with increasing temperature. At lower temperatures, the relatively small activation energy suggests that charge transport occurs predominantly through the correlated barrier hopping (CBH) mechanism, where localized charge carriers hop between defect states over potential barriers. In this region, the decrease in the exponent (*s*) with increasing temperature is characteristic of thermally activated hopping conduction. Above ~613 K, the increase in thermal energy enhances lattice vibrations and carrier-lattice interactions, leading to greater dynamic disorder within the structure. Under these conditions, the conduction process gradually shifts toward the non-small polaron tunneling (NSPT) mechanism, where charge carriers move *via* thermally assisted tunneling between localized states. The higher activation energy observed in this temperature region reflects the stronger carrier-lattice coupling associated with polaronic transport. Similar behavior has been widely reported for pyrophosphate-based solid electrolytes, where phase transitions are associated with modifications in ion-transport pathways at characteristic temperatures, as observed in compounds such as $NaGaP_2O_7$ (593 K),[37] $TlFeP_2O_7$ (593 K),[5] $LiCrP_2O_7$ (550 K),[11] $LiAlP_2O_7$ (600 K),[12] and $AgCrP_2O_7$ (583 K).[55] In the present compound, the conduction process is mainly attributed to the migration of Li^+ ions through structural tunnels extending along the *a*-axis (Fig. 2(b)), which likely plays a key role in the observed transport behavior.

Compared to other $LiM^{3+}P_2O_7$ pyrophosphate compounds reported in the literature, the investigated ceramic sample exhibits moderate ionic conductivity, as detailed in Table 4. Variations in conductivity among these materials can be largely attributed to differences in the ionic radius of the trivalent cation (M^{3+}) and its influence on the crystal lattice geometry and bonding environment. These structural factors, along with the nature and strength of electrostatic interactions within the framework, play a pivotal role in determining the efficiency of charge carrier migration, thereby directly impacting the overall ionic transport properties of the material.

3.6. Dielectric permittivity formalism analysis

The analysis of dielectric permittivity is a powerful tool for investigating the electrical properties of materials, particularly their polarization mechanisms.[58,59] A valuable insight into dipolar relaxation processes, interfacial polarization, and charge carrier dynamics can be gained by examining the frequency and temperature dependence of the real (ε') and imaginary (ε'') components of the complex permittivity. This method is particularly effective for identifying relaxation phenomena and evaluating conduction mechanisms, making it indispensable for characterizing the materials used in electronic devices, capacitors, and energy storage systems.[5,27,58–61] The real part of the dielectric constant (ε'), representing energy storage, and the imaginary part (ε''), associated with energy loss, can be calculated from the impedance components Z' and Z'' using the following equations:

$$\varepsilon' = \frac{Z''}{\omega C_0 (Z'^2 + Z''^2)} \quad (10)$$

$$\varepsilon'' = \frac{Z'}{\omega C_0 (Z'^2 + Z''^2)} \quad (11)$$

where C_0 refers to the vacuum capacitance ($C_0 = (\varepsilon_0 A)/d$), ε_0 refers to the permittivity of free space, and ω refers to the angular frequency.

Fig. 8 presents the frequency-dependent variation of the real (ε') and imaginary (ε'') parts of the dielectric permittivity of $LiGaP_2O_7$ over the studied temperature range. As shown in Fig. 8(a), ε' decreases progressively with increasing frequency across all temperatures, while maintaining significantly high values at lower frequencies, reaching up to approximately 6.32×10^4 at 673 K. The pronounced increase in ε' at low frequencies and elevated temperatures is a typical signature of interfacial (Maxwell–Wagner) polarization, which originates from space-charge accumulation at grain boundaries. This accumulation leads to the formation of localized potential barriers that hinder charge transport and, consequently, enhance the overall dielectric response. The relatively high ε' values obtained for $LiGaP_2O_7$ are comparable to those reported for other well-known pyrophosphate-based systems. At low frequencies, this interfacial polarization becomes dominant because charge carriers have sufficient time to migrate and accumulate at interfaces, producing a strong apparent increase in permittivity. In contrast, at higher frequencies, the effect of Maxwell–Wagner polarization is strongly suppressed since the charge carriers are unable to follow the rapidly alternating electric field, resulting in lower and more frequency-stable dielectric constant values that are more representative of the intrinsic dielectric behavior of the material.

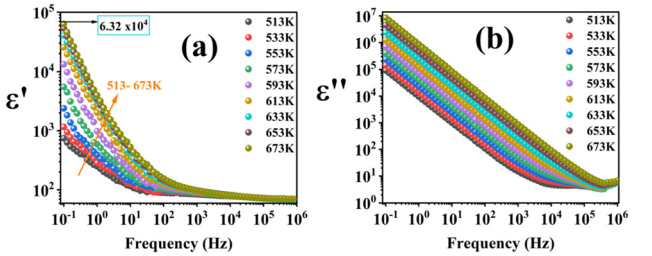

Fig. 8 (a) Real part and (b) imaginary part of the frequency-dependent dielectric permittivity.

The dielectric performance notably surpasses that of well-established materials such as $Li_2Cu_5(Si_2O_7)_2$,[61] which exhibits ε' values around 10^4 in the 673–833 K range and is recognized as a promising material for future energy-storage applications. The dielectric properties of $LiGaP_2O_7$ position it as a promising candidate for advanced technological applications, especially when compared to other members of the $A^+M^{3+}P_2O_7$ family. For instance, $AgCrP_2O_7$[55] displays ε' values up to 1.2×10^4 in the 523–673 K range, while $TlFeP_2O_7$ displays values as high as 3×10^4 in the range 473–673 K. These two compounds are both noted for their potential in low-frequency energy storage systems.[5] These comparisons highlight the promising potential of $LiGaP_2O_7$ for low-frequency dielectric and energy storage applications. The observed behavior of ε' is well described by the Maxwell–Wagner model and Koop's phenomenological theory.[61,62] As the frequency increases, the time scale becomes too short for interfacial charges to respond, reducing the contribution from this polarization mechanism. Consequently, ε' decreases with increasing frequency.

Fig. 8(b) displays the imaginary part of the permittivity (ε''), which also shows a monotonic decline with frequency across all temperatures. This trend is attributed to the inability of dipoles and mobile charge carriers to keep pace with the rapidly oscillating electric field at higher frequencies. At these frequencies, dielectric behavior becomes increasingly dominated by intrinsic processes such as ionic and electronic polarization within the grains, which contribute less significantly to permittivity than interfacial effects.[59,63] The reduction in ε'' is also influenced by decreased mobility of charge carriers and relaxation losses associated with Li^+ ion migration, dipolar reorientation, and carrier polarization. Although distinct dispersion features are apparent in the ε' spectra, such anomalies are less

Table 4 DC conductivity (σ_{dc}) and activation energy (E_a) of previously studied pyrophosphate compounds

Compounds	σ_{dc} (Ω^{-1} cm^{-1})	E_a (eV)	Ref.
$LiScP_2O_7$	$\approx 4 \times 10^{-7}$ (573 K)	1.06 (523–593 K)	56
$LiFeP_2O_7$	$\approx 8 \times 10^{-7}$ (573 K)	1.23 (473–690 K)	56
$LiAlP_2O_7$	$\approx 5 \times 10^{-6}$ (540 K)	0.84 (540–610 K)/0.93 (620–680 K)	12
$LiGdP_2O_7$	$\approx 4 \times 10^{-8}$ (523 K)	0.84 (473–773 K)	57
$LiCrP_2O_7$	$\approx 8 \times 10^{-7}$ (580 K)	0.49 (460–550 K)/0.91 (560–700 K)	11
$LiGaP_2O_7$	$\approx 2.28 \times 10^{-8}$ (573 K)	0.72 (513–593 K)/1.19 (613–673 K)	This work

prominent in the ε'' response. This is primarily due to the substantial contribution of DC conductivity at low frequencies, which leads to a steep rise in ε'' and obscures relaxation-related features.[64,65] As a result, precise analysis of relaxation dynamics based solely on ε'' is challenging. To address this limitation, it is advisable to employ complementary formalisms such as the complex electric modulus approach, which effectively suppresses the influence of electrode polarization and DC conductivity, providing a clearer picture of the material's intrinsic relaxation behavior.

3.7. Electrical modulus analysis

The electrical modulus formalism, widely employed in recent years to investigate ionic materials,[66,67] was used to analyze the relaxation behavior of the system. This approach characterizes the dielectric relaxation under an applied electric field at constant electric displacement, making it particularly effective for probing the dynamics of charge carriers in materials with significant long-range ionic motion. One of its main advantages lies in reducing the effects of electrode polarization, thereby enabling a more accurate assessment of intrinsic relaxation processes associated with ionic conduction.[68]

To evaluate the imaginary component of the electric modulus (M''), the following formula was applied:

$$M'' = \frac{\varepsilon'}{\varepsilon'^2 + \varepsilon''^2} \tag{12}$$

Fig. 9(a) presents the frequency-dependent variation of the imaginary part of the electric modulus (M'') for the $LiGaP_2O_7$ compound over the studied temperature range. At each temperature, the M'' spectra display a distinct relaxation peak at a specific frequency (denoted as f_r), indicating a transition in charge transport from short-range (localized) to long-range (delocalized) mechanisms.[69–71] In the low-frequency region (below f_r), the electrical conductivity is primarily governed by long-range hopping of charge carriers.[72,73] In the intermediate-frequency region (above f_r), the contribution of short-range hopping dynamics becomes more prominent.[73] In the high-frequency domain, charge carriers are confined to localized states, limiting their contribution to long-range conduction. As temperature increases, the M'' peak shifts toward higher frequencies and becomes increasingly asymmetric, reflecting enhanced thermal activation of charge carriers and a broader distribution of relaxation times. This temperature-dependent peak behavior and asymmetric shape are characteristic of a non-Debye relaxation process.

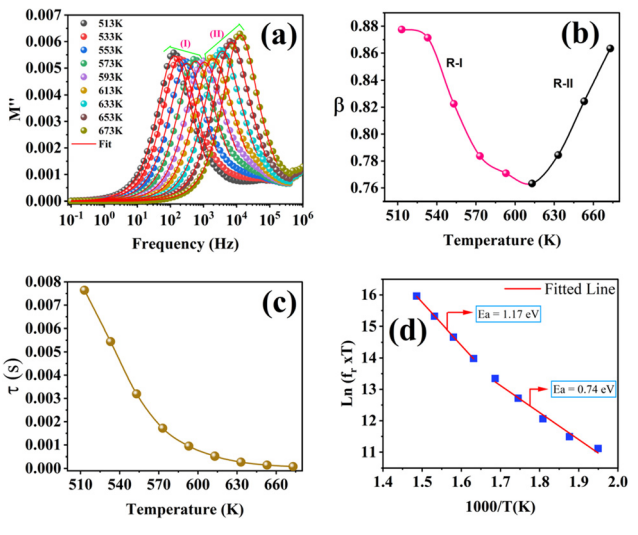

Fig. 9 (a) Imaginary part of the frequency-dependent electric modulus (M''). (b) Variation of the β parameter with temperature. (c) Temperature dependence of the relaxation time (τ). (d) Arrhenius plot of $\ln(f_r \cdot T)$ *versus* $1000/T$.

Furthermore, the appearance of two distinct relaxation regions, labeled (I) and (II), along with the observed shift in peak position, reinforces the change in conduction mechanism previously identified in the impedance analysis, suggesting a transition between different types of mobile charge carriers or transport pathways.

To gain further insight into the nature of this dielectric relaxation, the β parameter is determined from the frequency-dependent M'' data using the following expression:

$$M''(f) = \frac{M''_{max}(f)}{\left[1 - \beta + \left(\frac{\beta}{\beta+1}\right)\left[\beta\left(\frac{f_r}{f}\right) + \left(\frac{f}{f_r}\right)^{\beta}\right]\right]} \tag{13}$$

The term M''_{max} denotes the maximum value of $M''(f)$, which occurs at the peak of the relaxation process, while f_r refers to the frequency at which $M''(f)$ reaches its maximum. The exponent β ($0 < \beta \leq 1$) is a stretching exponent that characterizes the width and asymmetry of the relaxation peak. When $\beta = 1$, it corresponds to ideal Debye-type relaxation, indicating negligible dipole–dipole interactions. In contrast, when $\beta < 1$, it suggests pronounced dipolar interactions, characteristic of non-Debye relaxation processes.[74]

Fig. 9(b) illustrates the temperature dependence of the stretching exponent β, derived from fitting the M'' spectra using the Bergman formalism. The observed non-monotonic behavior, characterized by a V-shaped curve, reflects the complex nature of the relaxation dynamics. The initial decrease in β with increasing temperature indicates a broadening of the relaxation time distribution, likely due to growing disorder or the coexistence of multiple conduction pathways. The minimum in β, observed at 613 K, marks a transition point beyond which β rises again, suggesting the emergence of a more dominant and uniform conduction mechanism at higher temperatures. This evolution further supports the thermally activated nature of the charge transport and the non-Debye relaxation behavior throughout the investigated range.

Fig. 9(c) illustrates the temperature dependence of the relaxation time (τ), derived from the optimal fitting of the experimental M'' data. As the temperature increases, τ decreases significantly, indicating a thermally activated relaxation process. This behavior is primarily associated with ionic transport, possibly involving polaron hopping facilitated by local lattice vibrations, often referred to as "rattling" effects. The temperature-induced

reduction in τ reflects the enhanced mobility and progressive delocalization of charge carriers.[75,76] Moreover, this evolution is accompanied by a transition toward more homogeneous relaxation dynamics, as evidenced by the approach to dynamics of Debye-like behavior at higher temperatures, consistent with narrowing the distribution of relaxation times.

Fig. 9(d) illustrates the Arrhenius plot of the relaxation frequency (f_r), presented as $\ln(f_r \times T)$ *versus* $1000/T$, which reveals two distinct linear regions. In the first region (513–593 K), the slope yields an activation energy around 0.74 eV, while a higher activation energy of 1.17 eV is observed in the second region (613–673 K). This change suggests a transition in the dominant conduction mechanism as temperature increases. The good agreement between these activation energies and those obtained from DC conductivity indicates that the charge transport and relaxation phenomena in $LiGaP_2O_7$ are governed by similar thermally activated processes.[77]

4. Conclusion

In this study, the $LiGaP_2O_7$ compound was comprehensively investigated using powder X-ray diffraction (PXRD), scanning electron microscopy (SEM), Raman spectroscopy, and electrical impedance spectroscopy. Rietveld refinement confirmed that $LiGaP_2O_7$ crystallizes in a monoclinic structure with the space group $P2_1$, and a crystallite size of approximately 60 nm was estimated. SEM micrographs revealed an average grain size of about 2.49 μm, indicating that each grain is composed of multiple crystallites, thereby confirming the polycrystalline nature of the material. Raman spectroscopy further validated the presence of the $(P_2O_7)^{4-}$ diphosphate, consistent with the expected structural framework.

Impedance spectroscopy analysis revealed a single relaxation process with non-Debye behavior. Nyquist plots were successfully fitted using an equivalent circuit model, confirming grain boundary-dominated conduction. The AC conductivity followed Jonscher's universal power law, with a frequency exponent indicating a temperature-dependent transition in the charge transport mechanism. The conduction process was well described by the correlated barrier hopping (CBH) model in the 513–593 K range (activation energy $\approx$ 0.72 eV), while at higher temperatures (613–673 K), the non-overlapping small polaron tunneling (NSPT) model dominates with a higher activation energy of about 1.19 eV. Dielectric studies revealed strong frequency dispersion and high permittivity values at low frequencies, reaching approximately 6.32×10^4, which is attributed to interfacial (Maxwell–Wagner) polarization effects. The observed negative temperature coefficient of resistance (NTCR) behavior confirms thermally activated conduction in the system.

Collectively, $LiGaP_2O_7$ exhibits a combination of high dielectric response, thermally activated hopping conduction, and stable polycrystalline structure, making it a promising candidate for low-frequency dielectric devices, NTC thermistors, and energy-related applications. Its lithium content and thermal stability up to 673 K further suggest potential interest for future studies in solid-state electrochemical and electronic applications.

Author contributions

Imen Gharbi: writing – original draft, validation, software, methodology, and investigation. Iheb Garoui: writing – original draft, validation, software, methodology, and investigation. Souad Chkoundali: writing – original draft, visualization, and formal analysis. Nazir Mustapha: formal analysis, validation, writing review. Mokhtar Hjiri: writing – review & editing, validation, investigation, and formal analysis. Abderrazek Oueslati: writing – review & editing, visualization, validation, investigation, formal analysis, and data curation.

Conflicts of interest

The authors declare that they have no known competing financial interests or personal relationships that could have appeared to influence the work reported in this paper.

Data availability

The authors confirm that the data used to support the findings of this study are included within the article and are available from the corresponding author upon reasonable request.

Supplementary information (SI) is available. See DOI: https://doi.org/10.1039/d6ma00256k.

Acknowledgements

This work was supported and funded by the Deanship of Scientific Research at Imam Mohammad Ibn Saud Islamic University (IMSIU) (grant number IMSIU-DDRSP2602).

References

1 M. Hantech, R. Dhahri, E. Dhahri and B. F. O. Costa, Analysis of Structural, Electrical, and Magnetic Properties of Sr0.5Ca0.5Fe12O19 and Ba0.5Ca0.5Fe12O19 for Advanced Technological Application, *Ceram. Int.*, 2025, **51**(20), 31734–31746, DOI: 10.1016/j.ceramint.2025.04.364.
2 I. Soudani, M. Tliha, S. Znaidia, A. Oueslati, A. Aydi and K. Khirouni, Study on structural and conduction behavior of overlapping polaron tunnel of SrZnP2O7, *J. Solid State Chem.*, 2025, **341**, 125087, DOI: 10.1016/j.jssc.2024.125087.
3 S. Chkoundali, H. Ghoudi, S. Aydi, A. Oueslati and A. Aydi, Synthesis, morphology investigation and electrical conduction mechanism of rubidium yttrium diphosphate, *J. Aust. Ceram. Soc.*, 2025, **61**(3), 1101–1112, DOI: 10.1007/s41779-024-01138-z.
4 M. Karray, I. Garoui, S. Nasri, S. Znaidia, A. Mahmoud and A. Oueslati, Cesium Iron(III) Pyrophosphate Prepared Using a Solid-State Process: Structure, Mössbauer Spectroscopy,

and Relaxation Dynamics, *ChemistrySelect*, 2025, **10**(2), e202404727, DOI: 10.1002/slct.202404727.

5 I. Garoui, *et al.*, Dielectric Relaxation and Electrothermal Charge Carrier Transport *via* Correlated Barrier Hopping in the Solid Electrolyte TlFeP2O7: Experimental and Theoretical Modeling, *Ceram. Int.*, 2025, **51**(19), 29510–29525, DOI: 10.1016/j.ceramint.2025.04.155.

6 M.-H. Yu, D. Zhao, R.-J. Zhang and Q.-X. Yao, A novel sm3+ activated phosphor powder Ba2LiGa(P2O7)2 with orange–red luminescence and high color purity, *J. Mater. Sci.: Mater. Electron.*, 2023, **34**(32), 2170, DOI: 10.1007/s10854-023-11557-6.

7 A. T. Apostolov, I. N. Apostolova and J. M. Wesselinowa, Magnetic and electric properties of multiferroic LiFeP2O7. Comparison with LiCrP2O7, *Mod. Phys. Lett. B*, 2021, **35**(09), 2150158, DOI: 10.1142/s021798492150158x.

8 E. Pachoud, *et al.*, Top-Seeded Single-Crystal Growth, Structure, and Physical Properties of Polar LiCrP2O7, *Cryst. Growth Des.*, 2013, **13**(12), 5473–5480, DOI: 10.1021/cg401442r.

9 Z. Lu, *et al.*, LiGaP2O7:Cr3 +, Yb3+ phosphors for broadband NIR LEDs toward multiple applications, *J. Alloys Compd.*, 2023, **956**, 170311, DOI: 10.1016/j.jallcom.2023.170311.

10 S. Nasri, M. Megdiche and M. Gargouri, DC conductivity and study of AC electrical conduction mechanisms by non-overlapping small polaron tunneling model in LiFeP2O7 ceramic, *Ceram. Int.*, 2016, **42**(1), 943–951, DOI: 10.1016/j.ceramint.2015.09.023.

11 M. Sassi, A. Bettaibi, A. Oueslati, K. Khirouni and M. Gargouri, Electrical conduction mechanism and transport properties of LiCrP2O7 compound, *J. Alloys Compd.*, 2015, **649**, 642–648, DOI: 10.1016/j.jallcom.2015.07.148.

12 Y. B. Taher, A. Oueslati, K. Khirouni and M. Gargouri, Impedance spectroscopy and conduction mechanism of LiAlP2O7 material, *Mater. Res. Bull.*, 2016, **78**, 148–157, DOI: 10.1016/j.materresbull.2016.02.033.

13 M. S. Bhuvaneswari, S. Selvasekarapandian, O. Kamishima, J. Kawamura and T. Hattori, Structural and impedance analysis of $LiBiP_2O_7$, *J. Solid State Electrochem.*, 2005, **10**(7), 434–438, DOI: 10.1007/s10008-005-0009-7.

14 H. Yu, Z. Su and L. Wang, Synthesis and electrochemical properties of $LiVP_2O_7$/C as novel cathode material for lithium ion batteries, *Ceram. Int.*, 2017, **43**(18), 17116–17120, DOI: 10.1016/j.ceramint.2017.09.131.

15 R. D. Shannon, Revised effective ionic radii and systematic studies of interatomic distances in halides and chalcogenides, *Acta Crystallogr., Sect. A*, 1976, **32**(5), 751–767, DOI: 10.1107/s0567739476001551.

16 G. Bandoli, A. Dolmella, F. Tisato, M. Porchia and F. Refosco, Mononuclear six-coordinated Ga(III) complexes: A comprehensive survey, *Coord. Chem. Rev.*, 2009, **253**(1–2), 56–77, DOI: 10.1016/j.ccr.2007.12.001.

17 U. Hoppe, D. Ilieva and J. Neuefeindb, The Structure of Gallium Phosphate Glasses by High-energy X-ray Diffraction, *Z. Naturforsch., A:Phys. Sci.*, 2002, **57**(8), 709–715, DOI: 10.1515/zna-2002-0811.

18 Y. Li, *et al.*, $LiGaP_2O_7$: A Potential UV Nonlinear-Optical Crystal, *Inorg. Chem.*, 2019, **58**(10), 6597–6600, DOI: 10.1021/acs.inorgchem.9b00970.

19 H. Bih, I. Saadoune, H. Ehrenberg and H. Fuess, Crystal structure, magnetic and infrared spectroscopy studies of the LiCryFe1−yP2O7 solid solution, *J. Solid State Chem.*, 2009, **182**(4), 821–826, DOI: 10.1016/j.jssc.2009.01.005.

20 J. Barker, R. K. B. Gover, P. Burns and A. Bryan, $LiVP_2O_7$: A Viable Lithium-Ion Cathode Material?, *Electrochem. Solid-State Lett.*, 2005, **8**(9), A446, DOI: 10.1149/1.1979347.

21 I. V. Tertov, *et al.*, β-LiVP2O7 as a positive electrode material for Li-ion batteries, *Electrochim. Acta*, 2021, **389**, 138759, DOI: 10.1016/j.electacta.2021.138759.

22 J. Sakamoto, Super-ionic Conducting Oxide Electrolytes, *Handbook of Solid State Batteries*, 2015, pp. 391–414, DOI: 10.1142/9789814651905_0012.

23 M. Tatsumisago and A. Hayashi, Sulfide Glass-Ceramic Electrolytes for All-Solid-State Lithium and Sodium Batteries, *Int. J. Appl. Glass Sci.*, 2014, **5**(3), 226–235, DOI: 10.1111/ijag.12084.

24 V. Muenzel, *et al.*, A Comparative Testing Study of Commercial 18650-Format Lithium-Ion Battery Cells, *J. Electrochem. Soc.*, 2015, **162**(8), A1592–A1600, DOI: 10.1149/2.0721508jes.

25 S. Erol, Comparative Study of Impedance Spectroscopy Between Nickel-Metal Hydride and Lithium-ion Batteries, *Eur. J. Sci. Technol.*, 2021, (28), 144–151, DOI: 10.31590/ejosat.993325.

26 S. Jagtap, S. Rane, S. Gosavi and D. Amalnerkar, Study on I–V characteristics of lead free NTC thick film thermistor for self heating application, *Microelectron. Eng.*, 2011, **88**(1), 82–86, DOI: 10.1016/j.mee.2010.08.025.

27 Y. Moualhi, H. Rahmouni and F. Bahri, Doublet doped titanate ferroelectric system for capacitors and NTC thermistor applications, *Sens. Actuators, A*, 2024, **377**, 115596, DOI: 10.1016/j.sna.2024.115596.

28 L. H. Omari, L. Hajji, M. Haddad, T. Lamhasni and C. Jama, Synthesis, structural, optical and electrical properties of La-modified Lead Iron Titanate ceramics for NTCR thermoresistance based sensors, *Mater. Chem. Phys.*, 2019, **223**, 60–67, DOI: 10.1016/j.matchemphys.2018.10.035.

29 H. Zhao, B. Meng, Y. Wang and S. Zhao, A New Approach to Synthesize Nano-Sized SnO2 Via Low Temperature Solid-State Reaction, *J. Cluster Sci.*, 2025, **36**(3), 93, DOI: 10.1007/s10876-025-02813-2.

30 M. S. Sihotang, M. A. Angelo, M. Naibaho, M. Maulidita, N. Ichsan and M. Ginting, Effect of Barium Hexaferrite Doped Yttrium (Y^{3+}) On The Microwave Absorption By Solid-State Reaction Methods, *J. Technomaterial Phys.*, 2025, **7**(1), 063–070, DOI: 10.32734/jotp.v7i1.19265.

31 J. Rodríguez-Carvajal, Recent advances in magnetic structure determination by neutron powder diffraction, *Phys. B*, 1993, **192**(1–2), 55–69, DOI: 10.1016/0921-4526(93)90108-i.

32 I. Ragbaoui, S. Aydi, S. Chkoundali, M. Enneffati and A. Aydi, Effect of substitution on the structural, electrical properties, and dielectric relaxor behavior in lead-free

BiFeO3-based ceramics, *RSC Adv.*, 2024, **14**(2), 1330–1340, DOI: 10.1039/d3ra06962a.

33 M. Javed, *et al.*, Temperature dependent impedance spectroscopy and electrical transport mechanism in sol-gel derived MgCr2O4 spinel oxide, *Phys. B*, 2020, **599**, 412377, DOI: 10.1016/j.physb.2020.412377.

34 S. Ben Yahya, I. Garoui, M. Zaghrioui, A. Oueslati and B. Louati, Solid-state synthesized Li4GeO4 germanate: an exploration of its structure, vibrational characteristics, electrical conductivity, and dielectric properties, *RSC Adv.*, 2025, **15**(12), 9295–9304, DOI: 10.1039/d5ra01165e.

35 J. Belkouch, L. Monceaux, E. Bordes and P. Courtine, Comparative structural study of mixed metals pyrophosphates, *Mater. Res. Bull.*, 1995, **30**(2), 149–160, DOI: 10.1016/0025-5408(94)00128-6.

36 B. S. Parajón-Costa, R. C. Mercader and E. J. Baran, Spectroscopic characterization of mixed cation diphosphates of the type MIFeIIIP2O7 (with MI = Li, Na, K, Rb, Cs, Ag), *J. Phys. Chem. Solids*, 2013, **74**(2), 354–359, DOI: 10.1016/j.jpcs.2012.10.012.

37 R. Mendil, S. Nasri and A. Oueslati, Structural investigation, vibrational study, and Na-ion transport properties of NaGaP2O7 as sodium solid electrolyte, *Ionics*, 2025, **31**(3), 2501–2514, DOI: 10.1007/s11581-025-06087-6.

38 C. Julien, A. Ait Salah and F. Gendron, Synthesis and Characterization of Lithium Diphosphates LiFeP2O7 as Positive Electrodes for Lithium Batteries, *ECS Meet. Abstr.*, 2006, **MA2005-01**(35), 1343, DOI: 10.1149/ma2005-01/35/1343.

39 N. Ortega, *et al.*, Multiferroic properties of Pb(Zr,Ti)O3/CoFe2O4 composite thin films, *J. Appl. Phys.*, 2006, **100**, 12, DOI: 10.1063/1.2400795.

40 S. Karmakar, S. Varma and D. Behera, Investigation of structural and electrical transport properties of nanoflower shaped NiCo2O4 supercapacitor electrode materials, *J. Alloys Compd.*, 2018, **757**, 49–59, DOI: 10.1016/j.jallcom.2018.05.056.

41 P. Satpathy, A. Behera, S. Parhi and S. K. Parida, Electrical characterization of the barium manganite, *Mater. Today: Proc.*, 2022, **67**, 1180–1184, DOI: 10.1016/j.matpr.2022.07.453.

42 B. K. Das, T. Das and D. Das, Structural and electrical properties of mechanically alloyed ZnO nanoceramic for NTC thermistor application, *J. Mater. Sci.: Mater. Electron.*, 2023, **34**(3), 230, DOI: 10.1007/s10854-022-09670-z.

43 I. Garoui, *et al.*, Electronic Behavior, Charge-Carrier Transport Properties, and Dielectric Polarization of Lead-Free Sodium Metagermanate (Na2GeO3) Perovskite: Insights into Its Optoelectronic Potential, *J. Electron. Mater.*, 2026, **55**(6), 5143–5158, DOI: 10.1007/s11664-026-12813-1.

44 S. Ben Yahya, I. Garoui, A. Oueslati and B. Louati, Structural, Optical, and Conduction Relaxation Properties of TlCrP2O7 Driven by Nonoverlapping Small Polaron Tunneling, *ACS Omega*, 2026, **11**(4), 6227–6240, DOI: 10.1021/acsomega.5c10392.

45 S. Saha, K. L. Routray and A. Parida, Graphene-integrated Ag-doped $NiFe_2O_4$ nanostructures for high-performance supercapacitor application, *Diamond Relat. Mater.*, 2025, **155**, 112264, DOI: 10.1016/j.diamond.2025.112264.

46 S. Saha, K. L. Routray, P. Mahanandia and T. Ku Nayak, $ZnFe_2O_4$–CNT–graphene hybrid electrodes synthesized *via* Aloe vera-assisted route for high-performance supercapacitors, *Diamond Relat. Mater.*, 2026, **162**, 113242, DOI: 10.1016/j.diamond.2025.113242.

47 Y. Q. Gao, *et al.*, Structural and electrical properties of Mn1.56Co0.96Ni0.48O4 NTC thermistor films, *Mater. Sci. Eng., B*, 2014, **185**, 74–78, DOI: 10.1016/j.mseb.2014.02.011.

48 A. K. Jonscher, The 'universal' dielectric response, *Nature*, 1977, **267**(5613), 673–679, DOI: 10.1038/267673a0.

49 B. Louati, F. Hlel and K. Guidara, Ac electrical properties and dielectric relaxation of the new mixed crystal (Na0.8Ag0.2)2PbP2O7, *J. Alloys Compd.*, 2009, **486**(1–2), 299–303, DOI: 10.1016/j.jallcom.2009.06.148.

50 M. Rani, R. C. Pawar and N. Panwar, Exploring the comparison of optical, dielectric and photocatalytic performance of Yb3+ and Gd3+ half-doped DyCrO3 nanostructures, *Mater. Chem. Phys.*, 2024, **314**, 128848, DOI: 10.1016/j.matchemphys.2023.128848.

51 G. E. Pike, ac Conductivity of Scandium Oxide and a New Hopping Model for Conductivity, *Phys. Rev. B*, 1972, **6**(4), 1572–1580, DOI: 10.1103/physrevb.6.1572.

52 X. Le Cleac'h, Lois de variations et ordre de grandeur de la conductivité alternative des chalcogénures massifs non cristallins, *J. Phys.*, 1979, **40**(4), 417–428, DOI: 10.1051/jphys:01979004004041700.

53 F. Missaoui, *et al.*, Structural, dielectric and transport properties of NaxFe1/2Mn1/2O2 (x = 1 and 2/3), *RSC Adv.*, 2023, **13**(26), 17923–17934, DOI: 10.1039/d3ra02570e.

54 N. F. Mott, Conduction in glasses containing transition metal ions, *J. Non-Cryst. Solids*, 1968, **1**(1), 1–17, DOI: 10.1016/0022-3093(68)90002-1.

55 K. Akhrib, I. Gharbi, M. Sassi, M. Tliha, M. Ben Gzaiel and A. Oueslati, Electrical transport and dielectric relaxation mechanisms in AgCrP2O7: Synthesis and characterization, *J. Mol. Struct.*, 2025, **1333**, 141727, DOI: 10.1016/j.molstruc.2025.141727.

56 Ģ. Vītiņš, Z. Kaņepe, A. Vītiņš, J. Ronis, A. Dindūne and A. Lūsis, Structural and conductivity studies in LiFeP 2 O 7, LiScP 2 O 7, and NaScP 2 O 7, *J. Solid State Electrochem.*, 2000, **4**(3), 146–152, DOI: 10.1007/s100080050012.

57 G. Hirankumar, M. Vijayakumar and S. Selvasekarapandian, Synthesis and Electrical Characterization of Gd doped Lithium Phosphate, *Solid State Ionics*, 2002, 605–612, DOI: 10.1142/9789812776259_0071.

58 Y. Zidi, *et al.*, Experimental and theoretical perspective on band gap modulation in Sr2+ modified BaTiO3 capacitors, *Ceram. Int.*, 2025, **51**(13), 18166–18177, DOI: 10.1016/j.ceramint.2025.01.591.

59 M. Javed, Y. Moualhi, N. Akbar, A. Masood, T. Alomayri and S. A. Muhammed Ali, Electrical dynamics and Havriliak-Negami dielectric relaxation behavior of FeNi2O4 electromagnetic spinel nickelate, *Ceram. Int.*, 2025, **51**(19), 28109–28121, DOI: 10.1016/j.ceramint.2025.04.025.

60 X. Chen, W. Guo, R. Li, P. Du, X. Zhan and S. Gao, Structure, Electrochemical, and Transport Properties of Li- and F-Modified P2-Na2/3Ni1/3Mn2/3O2 Cathode Materials for Na-Ion Batteries, *Coatings*, 2023, **13**(3), 626, DOI: 10.3390/coatings13030626.

61 K. S. Chikara, A. K. Bera, A. Kumar and S. M. Yusuf, Li-Ion Conduction Mechanism and Relaxation Dynamics in Sorosilicate Compound Li2Cu5(Si2O7)2, *ACS Appl. Electron. Mater.*, 2023, **5**(9), 5137–5150, DOI: 10.1021/acsaelm.3c00868.

62 A. Radoń, D. Łukowiec, M. Kremzer, J. Mikuła and P. Włodarczyk, Electrical Conduction Mechanism and Dielectric Properties of Spherical Shaped Fe3O4 Nanoparticles Synthesized by Co-Precipitation Method, *Materials*, 2018, **11**(5), 735, DOI: 10.3390/ma11050735.

63 S. Sarkar, P. Saha, M. Kundu, S. Chakraborty and K. Mandal, Morphology dependent negative dielectric permittivity in spinel ferrite nanostructures, *J. Alloys Compd.*, 2024, **978**, 173513, DOI: 10.1016/j.jallcom.2024.173513.

64 A. Molak, M. Paluch, S. Pawlus, Z. Ujma, M. Pawełczyk and I. Gruszka, Properties of (Bi1/9Na2/3)(Mn1/3Nb2/3)O3analysed within dielectric permittivity, conductivity, electric modulus and derivative techniques approach, *Phase Transitions*, 2006, **79**(6–7), 447–460, DOI: 10.1080/01411590600892336.

65 S. Pawlus, S. Hensel-Bielowka, K. Grzybowska, J. Zioło and M. Paluch, Temperature behavior of secondary relaxation dynamics in tripropylene glycol, *Phys. Rev. B:Condens. Matter Mater. Phys.*, 2005, **71**, 17, DOI: 10.1103/physrevb.71.174107.

66 Y. Moualhi, M. Smari, H. Nasri and H. Rahmouni, Combined transport and dielectric models and experimental characterization based on impedance spectroscopy for studying the microstructural and transport properties of electro-ceramic perovskites, *Mater. Today Commun.*, 2024, **38**, 108529, DOI: 10.1016/j.mtcomm.2024.108529.

67 K. S. Chikara, A. K. Bera, A. Kumar and S. M. Yusuf, Role of Crystal Structure on the Ionic Conduction and Electrical Properties of Germanate Compounds A2Cu3Ge4O12 (A = Na, K), *ACS Appl. Electron. Mater.*, 2023, **5**(5), 2704–2717, DOI: 10.1021/acsaelm.3c00176.

68 S. I. Al-Saeedi, *et al.*, Green biopolymer and plasticizer for solid electrolyte preparation: FTIR, electrochemical properties and EDLC characteristics, *Arabian J. Chem.*, 2023, **16**(9), 105046, DOI: 10.1016/j.arabjc.2023.105046.

69 K. Yadagiri and R. Nithya, Rare earth manganite: a.c. electrical properties of Dy1−xKxMnO3 (x = 0.1, 0.2), *J. Mater. Sci.: Mater. Electron.*, 2019, **30**(10), 9973–9982, DOI: 10.1007/s10854-019-01338-5.

70 T. Jadli, Y. Moualhi, A. Mleiki, H. Rahmouni, K. Khirouni and A. Cheikhrouhou, Electrical and dielectric properties of Sm0.55Sr0.45MnO3 compound, *J. Solid State Chem.*, 2021, **302**, 122378, DOI: 10.1016/j.jssc.2021.122378.

71 S. Sharma, K. Shamim, A. Ranjan, R. Rai, P. Kumari and S. Sinha, Impedance and modulus spectroscopy characterization of lead free barium titanate ferroelectric ceramics, *Ceram. Int.*, 2015, **41**(6), 713–7722, DOI: 10.1016/j.ceramint.2015.02.102.

72 R. Gerhardt, Impedance and dielectric spectroscopy revisited: Distinguishing localized relaxation from long-range conductivity, *J. Phys. Chem. Solids*, 1994, **55**(12), 1491–1506, DOI: 10.1016/0022-3697(94)90575-4.

73 L. Zhang, Y. Pu and M. Chen, Complex impedance spectroscopy for capacitive energy-storage ceramics: a review and prospects, *Mater. Today Chem.*, 2023, **28**, 101353, DOI: 10.1016/j.mtchem.2022.101353.

74 S. Chkoundali, I. Garoui, W. Trigui and A. Oueslati, Crystal structure, Hirshfeld surface analysis, conduction mechanism and electrical modulus study of the new organic–inorganic compound [C8H10NO]2HgBr4, *RSC Adv.*, 2024, **14**(13), 8971–8980, DOI: 10.1039/d4ra00689e.

75 S. Nasri, A. Jraba, I. Garoui, A. Oueslati and E. Elaloui, Potassium tin chloride (K2SnCl6) as a lead-free perovskite: anti-solvent synthesis, structural characterization, and charge transport properties, *RSC Adv.*, 2025, **15**(7), 5369–5380, DOI: 10.1039/d5ra00090d.

76 M. ben gzaiel, I. Garoui, F. N. Almutairi, I. Mbarek and O. A, Lead-Free halide perovskites for optoelectronic application: Investigation of structural, optical, electric and dielectric behaviors, *Opt. Mater.*, 2024, **154**, 115664, DOI: 10.1016/j.optmat.2024.115664.

77 I. Garoui, M. Mallek, F. N. Almutairi, W. Rekik and A. Oueslati, Synthesis, Structural characterization and complex impedance analysis of a novel organic-inorganic hybrid compound based on Mercury(II) chloride, *J. Mol. Struct.*, 2024, **1315**, 138881, DOI: 10.1016/j.molstruc.2024.138881.